VSP imaging of CO_2 injection with rapid-repeat time lapse full waveform inversion

Xiaohui Cai, Kris Innanen, Qi Hu, Matt Eaid, Scott Keating, Kevin Hall, and Don Lawton

ABSTRACT

In order to monitor CO_2 transient change, we use elastic full waveform inversion (FWI) to detect the anomaly from rapid-repeat time-lapse VSP data. We implement both a P-wave velocity single-parameter inversion and a multi-parameter inversion, where effective source estimation and time-lapse strategy are introduced. The elastic FWI workflow is presented for identifying and estimating time-lapse changes introduced by injection of CO_2 at a depth of 300 m, and applying the workflow to field data shows that our time-lapse inversion scheme is able to detect and quantify the time-lapse anomaly. The inversion of a synthetic data also demonstrates the effectiveness of our time-lapse inversion scheme.

INTRODUCTION

Carbon capture and storage (CCS) is broadly recognized as having the potential to play a key role in meeting climate change targets. A major concern for CCS is the possibility for CO_2 to escape from the desired reservoir, accumulate in near surface reservoirs, and then escape into the atmosphere. The 2D time-lapse FWI can provide high-resolution models of physical properties of the subsurface, detecting and quantifying the anomaly in velocities, and monitoring injected CO_2 change (Egorov et al., 2017).

This year, the Containment and Monitoring Institute (CaMI) Newell County Facility in Alberta, which is part of Carbon Management Canada (CMC), carried out a rapid-repeat time-lapse VSP seismic experiment (named Tiny bubbles) (Innanen et al., 2019). In contrast to standard time-lapse surveys, the experiment specifically seeks anomaly which appear in the short term. In this report, the 3C geophone data and DAS data are used in FWI to support the estimation of subsurface parameter distributions for the rapid-repeat time-lapse survey.

WORKFLOW

Frequency-domain elastic FWI

Log-derived P-wave velocity single-parameter inversion

Our rapid-repeat time-lapse VSP inversion workflow mainly follows frequency FWI technology. We perform the 2D elastic frequency-domain FWI algorithm with the combined geophone and DAS data (Eaid et al., 2021a). The field data is accompanied by a suite of well logs, and this well log suite (Hu and Innanen, 2019) includes P-wave and S-wave sonic, and density logs, offering prior information about the P-wave velocity ($V_{\rm p}$), S-wave velocity ($V_{\rm s}$), and density (ρ) in the vicinity of observation well 2. Figure 1 shows the relationship between $V_{\rm p}$, $V_{\rm s}$, and ρ. Based on the the strong correlation between $V_{\rm p}$, $V_{\rm s}$, and ρ, we use the single parameter $V_{\rm p}$ to implement the 2D elastic frequency-domain FWI,

which could apply the prior information in the inversion and helps prevent cross-talk by only allowing updates in one parameter. The shear velocity and density could be obtained by the relationship in Figure 1. The initial model is obtained by smoothing the velocity log (Figure 2).

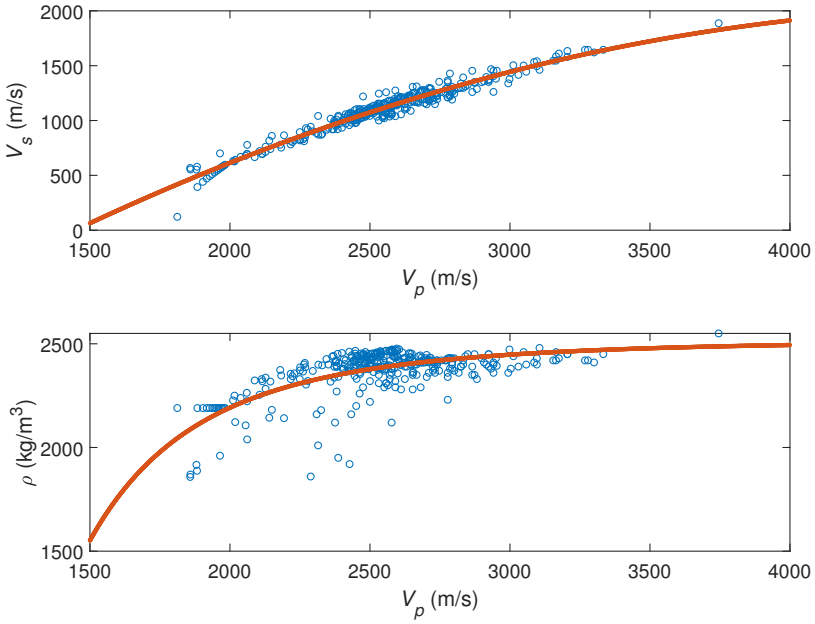

FIG. 1. The relationship between V_{p}, V_{s}, and ρ, and the solid red lines indicating the trend lines.

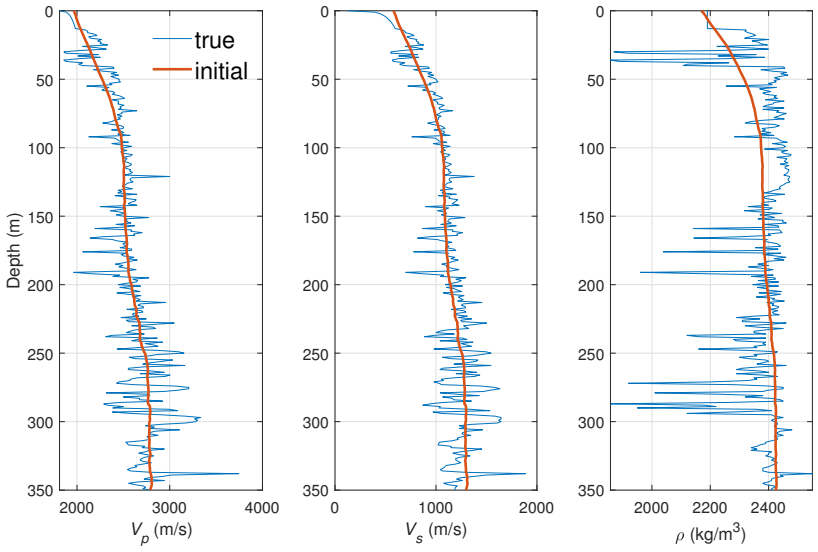

FIG. 2. The intial model achieved by the smooth of the log velocity.

Multi-parameter inversion

The single-parameter inversion could improve the convergence of inversions, but it also causes a loss of elasticity information in the result that is important for reservoir property

characterization. In addition, the assumption made for this parameterization, namely the model variables such as velocity and density are perfectly correlated, introduces uncertainty to the inversion. Thus, we also implement three-parameter elastic FWI.

Effective source estimation

A number of schemes can be applied for selecting a proper source wavelet for the inversion. Pratt (1999) and Roberts et al. (2008) introduce different source wavelet inversion algorithms in frequency domain and successfully used them for the inversion of experimental data. In our current study, to avoid the near surface from the inversion problem, we use the effective sources approach (Keating et al., 2021) for VSP FWI.

Time-Lapse Strategy

There are different inversion strategies that can be used to estimate the time-lapse changes in the medium, such as Parallel strategy, Sequential strategy, Double-difference strategy (Asnaashari et al., 2015). For the field data set here, rapid-repeat time-lapse data is characterized by multiple repetitions in a short period of time. During the time, main change is the injection behavior of CO_2 around 300 m. Therefore, the differences between the baseline and monitor data are mainly caused by the changes in the medium, while the changes due to the differences in source and receiver could be negligible. Here, we adopt the Parallel strategy. Moreover, both the baseline and the monitor inversions use the same inversion parameters and the same effective source energy.

FIELD DATA INVERSION

Background

In January 2022, the CaMI Newell County Facility, which is part of CMC, carried out a rapid-repeat time-lapse VSP seismic experiment (named Tiny bubbles) near Brooks, Alberta. The CO_2 was injected into a shallow formation, located at Upper Cretaceous Basal Belly River sandstone unit at a depth of 300 meters (Isaac and Lawton, 2016), and repeat a seismic shot whose ray-paths crossed the expected fluid, seeking evidence of transient changes. Geometry of the experiment is summarized in Figure 3. The CO_2 entered the Basal Belly River Sandstone (BBRS) formation, forming pressure and fluid plumes between depths of 290-305 m. The 24 3C geophones located from 190 m to 305 m with space interval of 5 m, while the DAS fiber located from 0 m to 337 m, where the DAS fiber data above 80 m has been muted. The source is 215 m away from the observation well, and injection well located between the source and observation well with 20 m offset from the observation well. In addition, the estimated pressure plume located at injection well at 267 m. Based on the rapid-repeat seismic shot, about 20 shots with good repeatability (Innanen et al., 2019) in a short period of time are grouped into a cluster, and there are 64 clusters in total. We process the data in clusters.

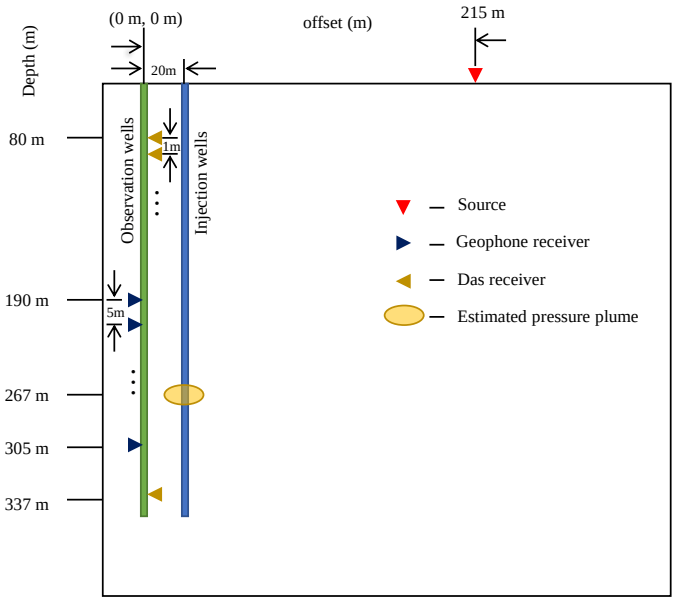

FIG. 3. Geometry of Tiny bubbles seismic source, injection and observation wells.

Preprocessing

Minimal preprocessing is performed before the inversion, where the preprocessing workflow has shown in Figure 4. For 2D FWI, orientation of three-component geophone VSP data into radial and vertical components is required, which is accomplished by QC Hodogram Display in Vista software. For DAS data ,we develop a depth register method to get the DAS data location, where the details can be seen in Cai et al. (2022).

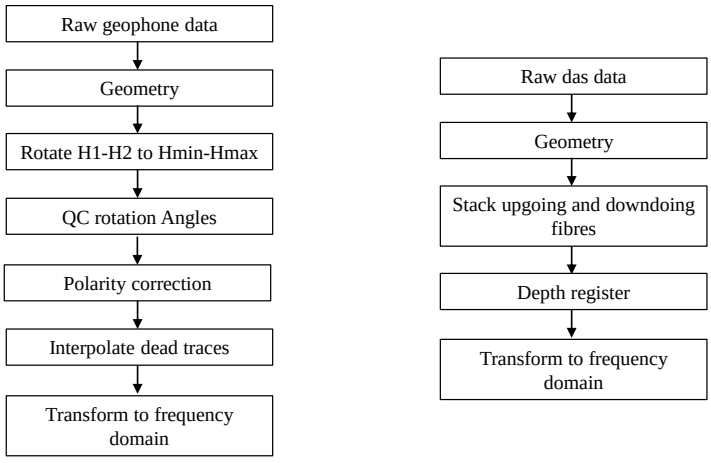

FIG. 4. Preprocessing workflow of the geophone data (left) and DAS data (right).

Dataset overview

Figure 5 shows the pressure change at 267 m (estimated pressure plume in Figure 3) from Jan 17 to Jan 22, 2022. The black circles are the times at which all 64 monitoring shot clusters occurred. Red squares and green squares indicate the first and second time CO_2 injection, respectively. From Figure 5, the pressure increase with the injection procedure and then relax. There are 64 clusters during the time, and we select the 10 clusters data (cluster 1, 3, 5, 13, 22, 31, 39, 47, 56, 64) to display the field data and their analysis, conveniently. The selected 10 clusters have their features:

1) cluster 1 is defined as the baseline data;
2) cluster 3 is near cluster 1;
3) the time of cluster 5 is around the beginning of the first CO_2 injection;
4) the time of cluster 13 is during the first CO_2 injection.
5) the time of cluster 22 is at the end of the first CO_2 injection;
6) the time of cluster 31 is between the twice CO_2 injection;
7) the time of cluster 39 is around the beginning of the second CO_2 injection;
8) the time of cluster 47 is during the second CO_2 injection.
9) the time of cluster 56 is at the end of the second CO_2 injection;
10) cluster 64 is the end.

To analyze the field data, we compare the monitor data with the baseline data (Figure 6). Figure 7 and Figure 8 show the monitor data (cluster 3 and cluster 39) and their differences with the baseline data for geophone vertical component, geophone horizontal component and DAS data. From the comparison in figures, we can see that the cluster 3 data have similar energy to baseline cluster 1 data, while the cluster 39 data diffs more from the baseline cluster 1 data. To quantitative analyze the difference between monitor clusters and baseline cluster, we calculate the normalization of their differences between the monitor and baseline data for geophone vertical component (Figure 9), geophone horizontal component (Figure 10) and DAS data (Figure 11). It can be seen from the normalization figures, the anomaly values appear around 285 m and 300 m in vertical component, and almost appear 285-290 m in horizontal component. The DAS normalized value does not show significant difference.

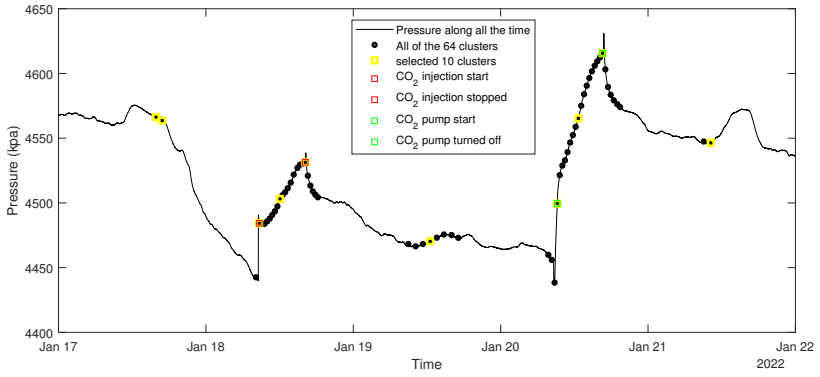

FIG. 5. Pressure change at 267 m (black curve) along the time from Jan 17 to Jan 22, 2022. Black circles are the times at which all 64 monitoring shot clusters occurred. Red squares and green squares indicate the first and second time CO_2 injection, respectively.

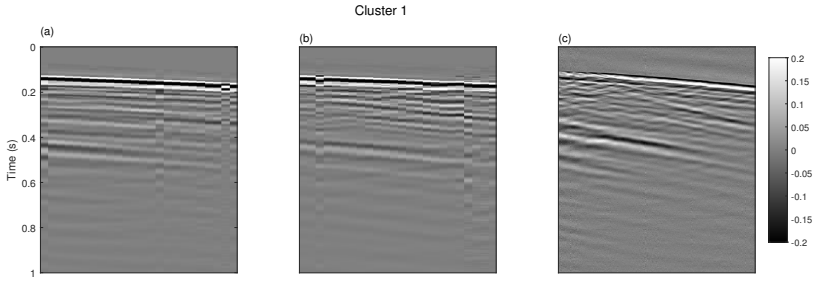

FIG. 6. The cluster 1 field data (baseline data) after preprocessing.(a)-(c) are the geophone vertical component, geophone horizontal component and DAS data, respectively.

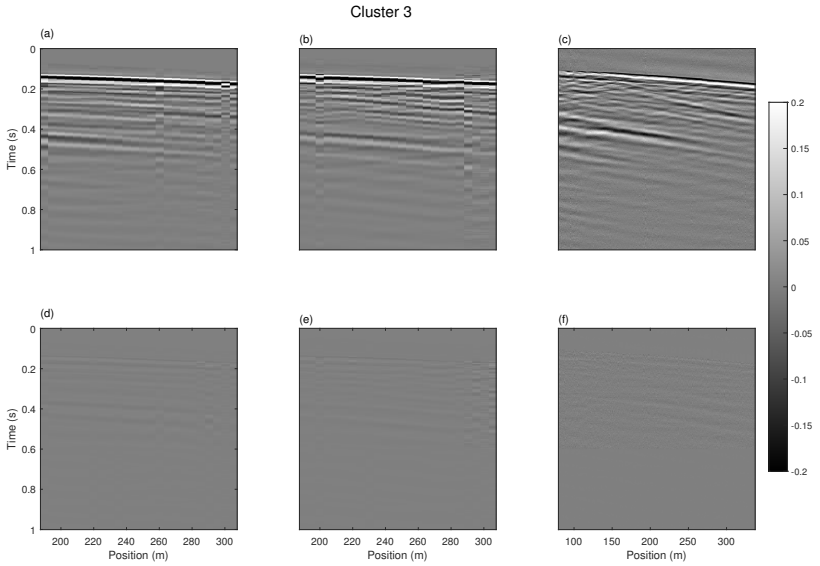

FIG. 7. (a)-(c) the cluster 3 field data (monitor data) after preprocessing. (d)-(f) difference between cluster 3 and cluster 1 field data. (a) and (d) the geophone vertical component, (b) and (e) geophone horizontal component, (c) and (f)) the DAS data.

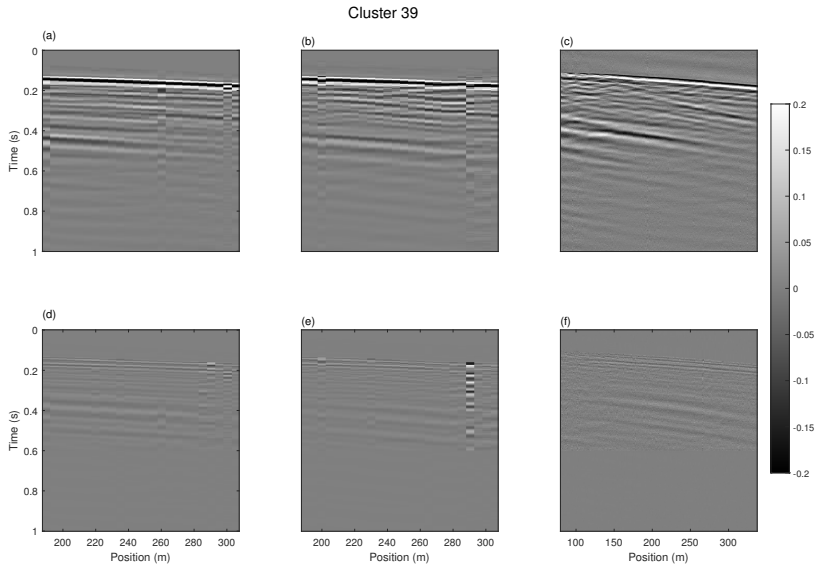

FIG. 8. (a)-(c) the cluster 39 field data (monitor data) after preprocessing. (d)-(f) difference between cluster 39 and cluster 1 field data. (a) and (d) the geophone vertical component, (b) and (e) geophone horizontal component, (c) and (f)) the DAS data.

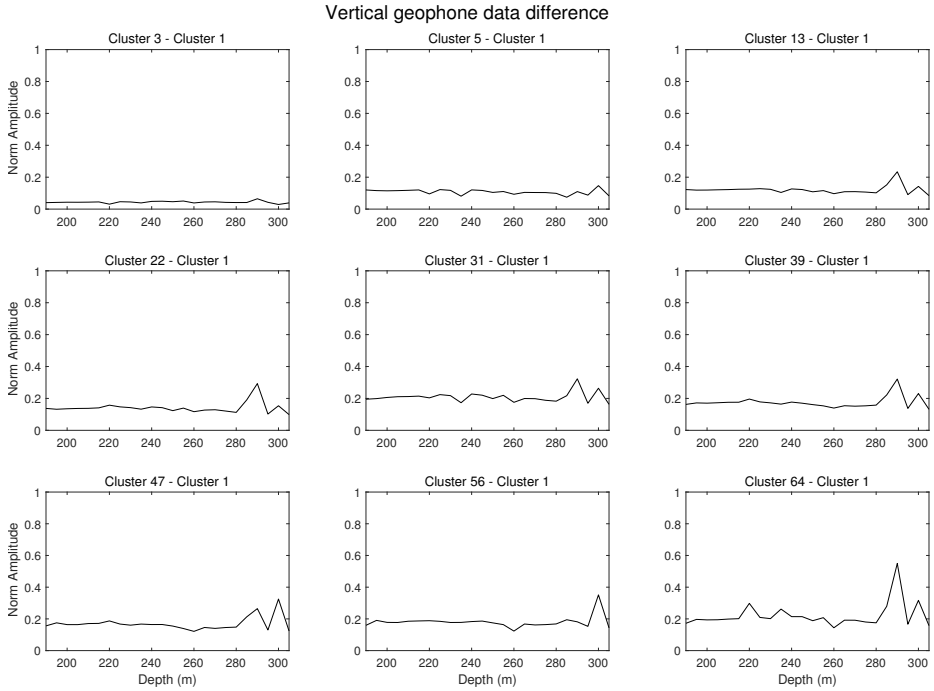

FIG. 9. The normalization of difference between monitor data (the selected clusters in Figure 5) and baseline data for geophone vertical component.

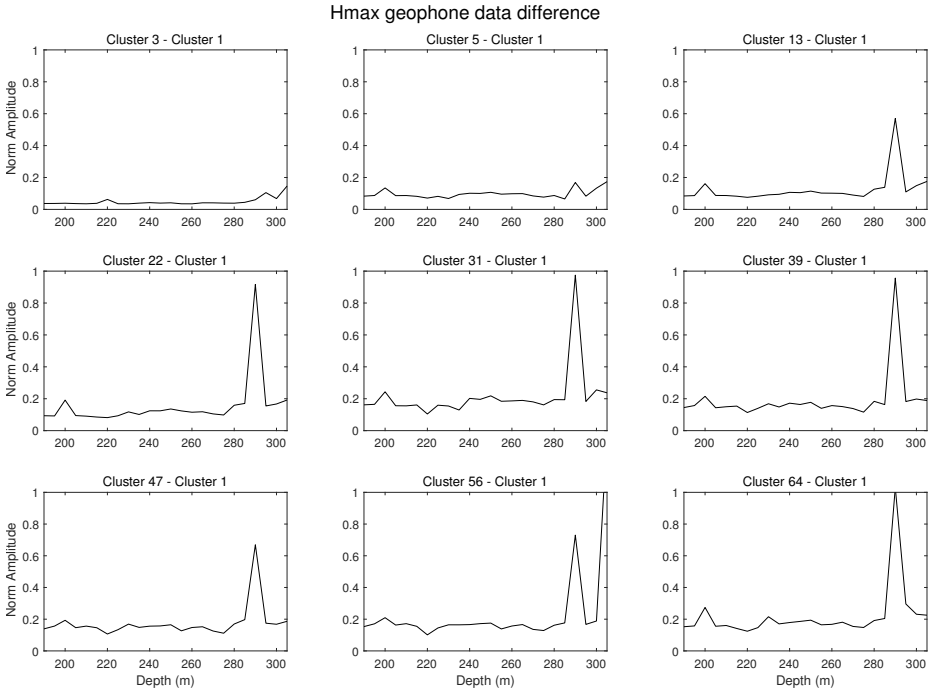

FIG. 10. The normalization of difference between monitor data (the selected clusters in Figure 5) and baseline data for geophone horizontal component.

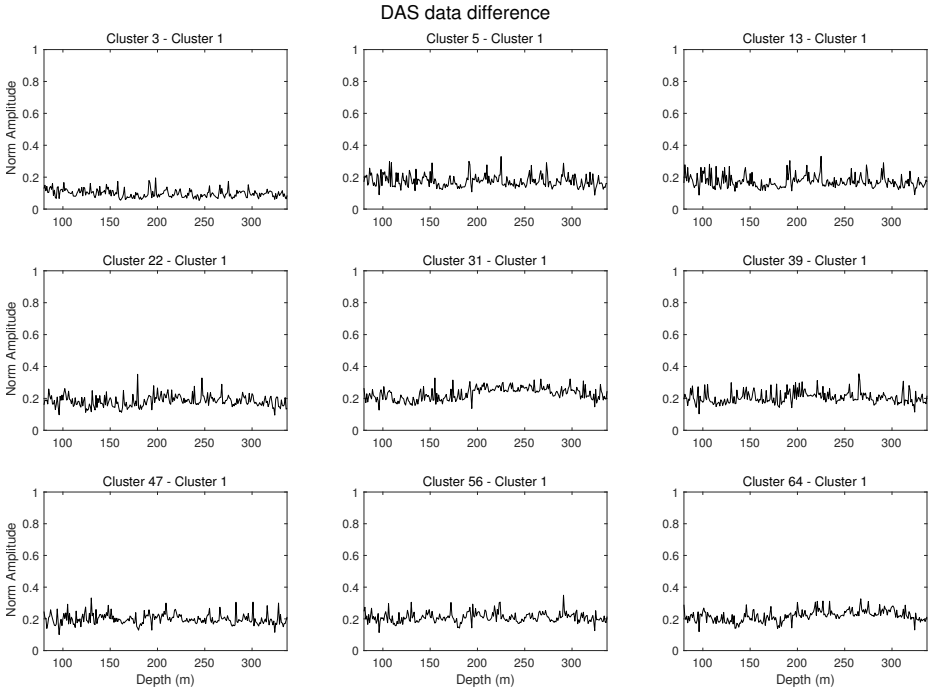

FIG. 11. The normalization of difference between monitor DAS data (the selected clusters in Figure 5) and baseline DAS data.

Inversion

Here, we use P-wave velocity single-parameter inversion and effective source estimation schemes to implement the elastic properties inversion. The model size is 240 m in the x-direction and 350 m in the z-direction, and the space interval is 2.5 m. In this report, we focus on frequencies between 10 Hz and 25 Hz. For the inversion, we consider five frequency bands, each consisting of seven frequencies, starting with the lowest frequencies and ending with a band spanning from low to high frequencies. The inversion approach could be divided into two steps: first is the source-only inversion based on baseline data and second is the model-only inversion for all of the 64 clusters data. Based on the strategy, both of monitor inversion and baseline inversion use the same effective source. For our implementation of the effective sources inversion strategy, we consider an effective source depth of 40 m. Figure 12 plots the theoretical energy profile for an explosive source using the baseline field shot geometry and monitor (cluster 3) energy profile for the inverted effective source after the 10 iterations of L-BFGS using the initial model (zero amplitude). The expected and inverted profiles are consistent providing a good source initialization. Figure 13 shows the real part of the measured data and modeled data, after the source-only updates and after the whole inversion process. The comparison demonstrate that the data-fit is relatively good after inversion. After source-only updates, we recalculate the amplitude scaling terms and proceed to model inversion. The inversion is performed over five frequency bands, with 10 iterations of L-BFGS optimization used at each band.

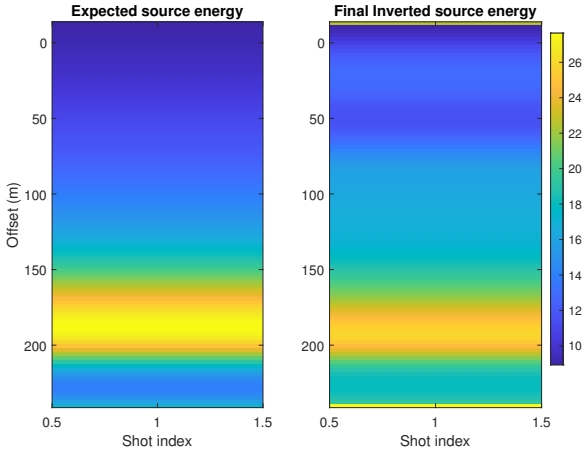

FIG. 12. Theoretical expected energy profile for an explosive source using the field shot geometry (cluster 1) (left) and energy for the inverted effective source (cluster 3) (right).

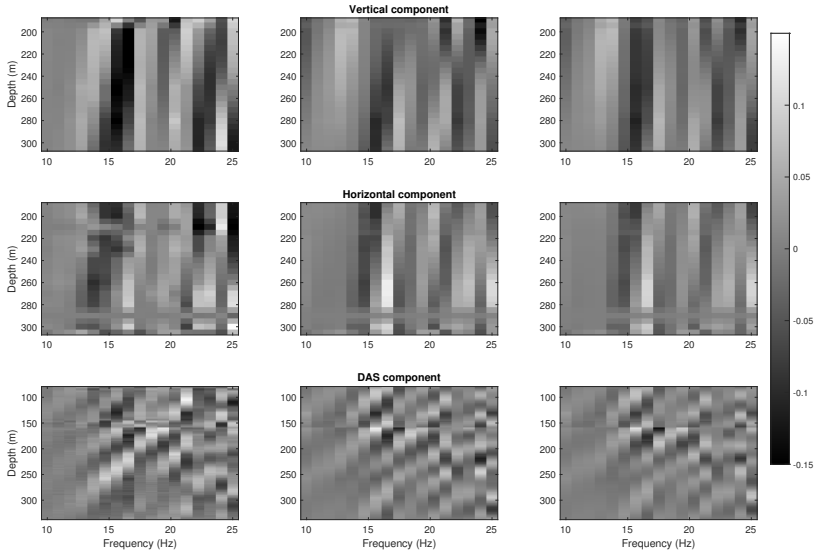

FIG. 13. Real part of frequency domain data for shot. Top row: vertical component of measurements. Middle row: horizontal component of measurements. Bottom row:DAS data measurements. Left column: Field data data. Middle column: Modeled data after effective source estimation. Right column: Modeled data after elastic properties.

The Figure 14 shows the initial and inverted models of V_{p}, V_{s}, and ρ for baseline data, while the Figure 15 indicates inverted V_{p} models for the other 9 selected monitor data in Figure 5. We use the single-parameter inversion method, the model of V_{s} and ρ has relationship with the V_{p}, so we mainly display the inverted V_{p} model. Figure 16 show the time-lapse V_{p} models between the monitor data and baseline data. It can be seen from the Figure 14 and Figure 15, the 10 inverted model seem consistent, and Figure 16 shows that the amplitude of time-lapse anomaly is different from the noise and the time-lapse anomaly located around 287.5 m instead of 300 m (injection location), which have a good consistency with the field data normalization in Figure 9 and Figure 10. Base on the phenomenon, we extract the inversion time-lapse V_{p} model value located (25 m, 287.5 m) for all 64 clusters. Figure 17 shows pressure data and inverted time-lapse V_{p} models for all of the 64 clusters. It can be seen that the inverted V_{p} keep decreasing with the first CO_2 injection, and then it reaches a relatively stable stage, there is a certain ups and downs during the second CO_2 injection, and the overall trend is downward, finally it tries to return to initial state. The time-lapse V_{p} anomaly varies between 0 and 150 m. Figure 18 indicates the comparison of the initial and inverted velocities models with the well logs data. The inverted model has a relative good consistent trend with log data after 230 m, and the difference is significant before 230 m, which may result from the only one source and limited geophone geometry (190 m to 305 m with 5 m interval).

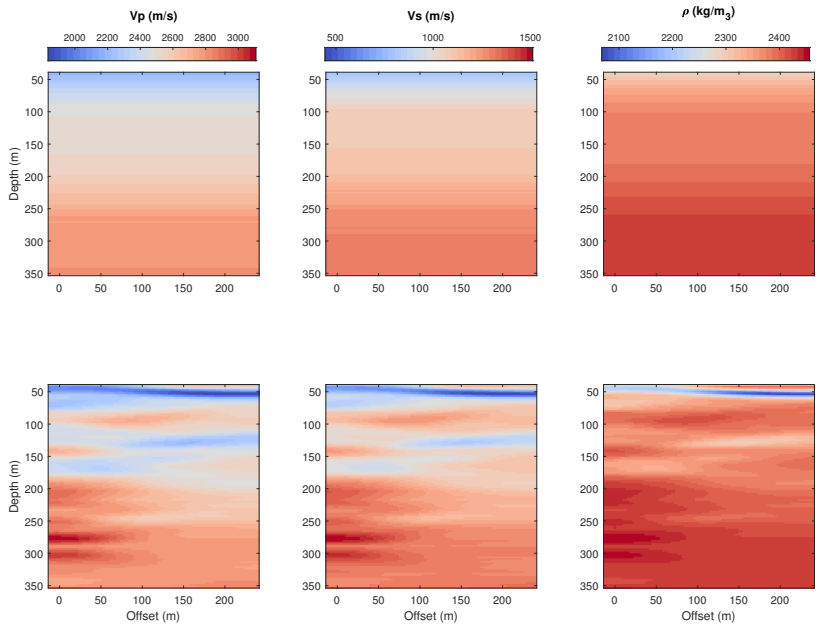

FIG. 14. Initial and inverted models of V_{p}, V_{s}, and ρ for cluster 1 (baseline data).

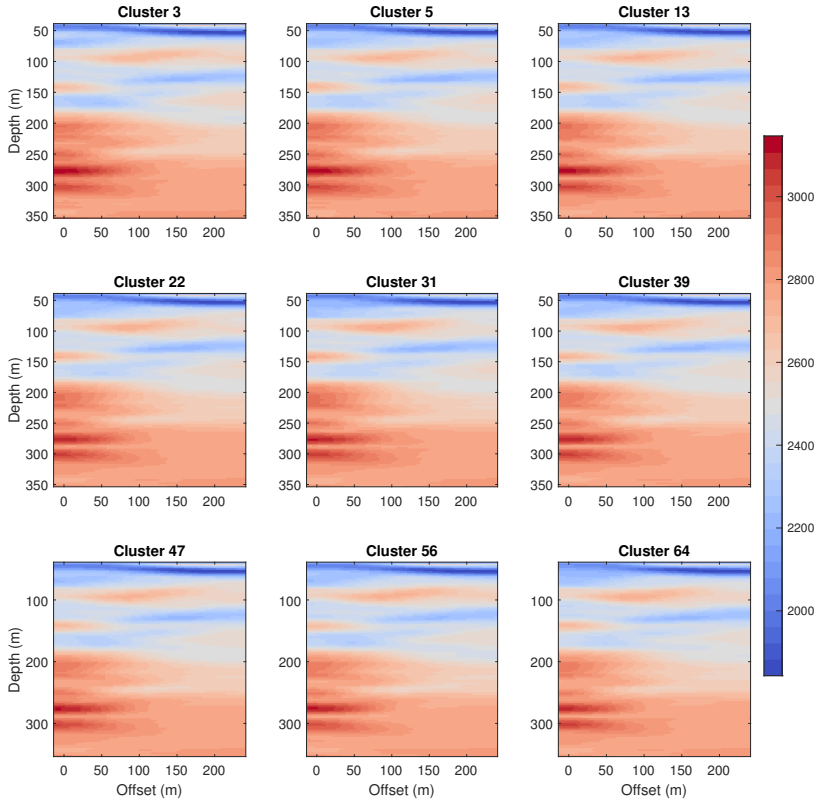

FIG. 15. The inverted V_{p} models for the 9 monitor data.

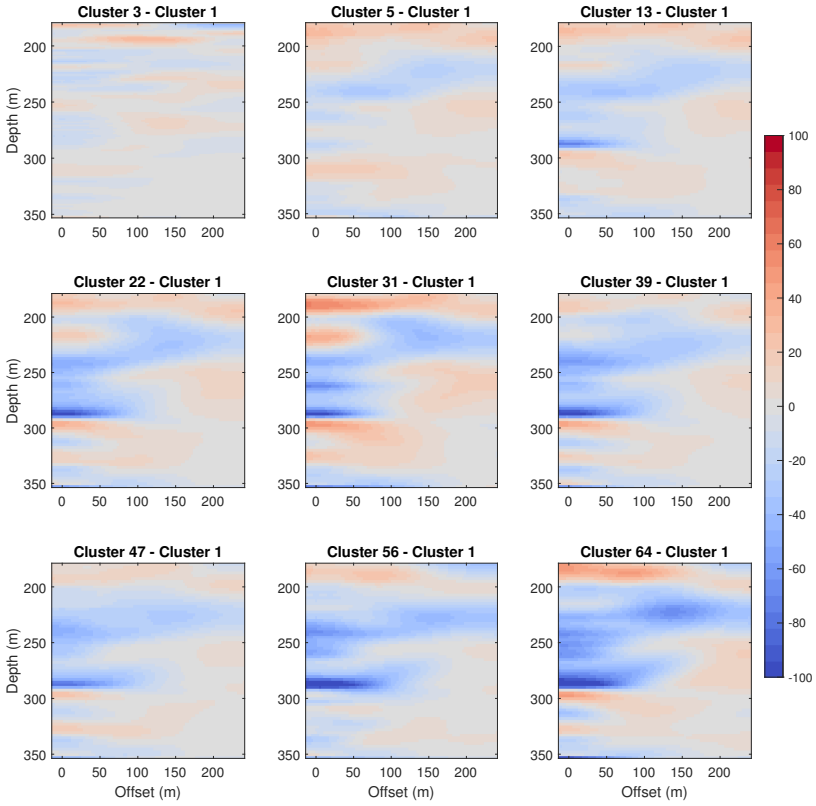

FIG. 16. The inverted V_{p} models difference between the 9 monitor data and baseline.

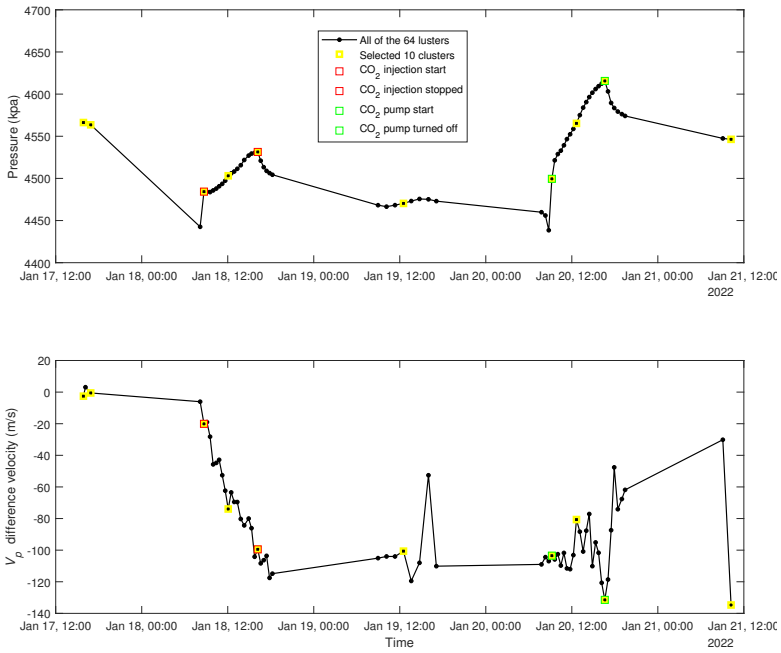

FIG. 17. Top rows: Pressure data at 267 m (black curve) for the 64 clusters. Bottom rows: The inverted V_{p} models difference between the 64 clusters and baseline data at 287.5 m. Yellow square are the 10 selected clusters. Red squares and green squares indicate the first and second CO_2 injection, respectively.

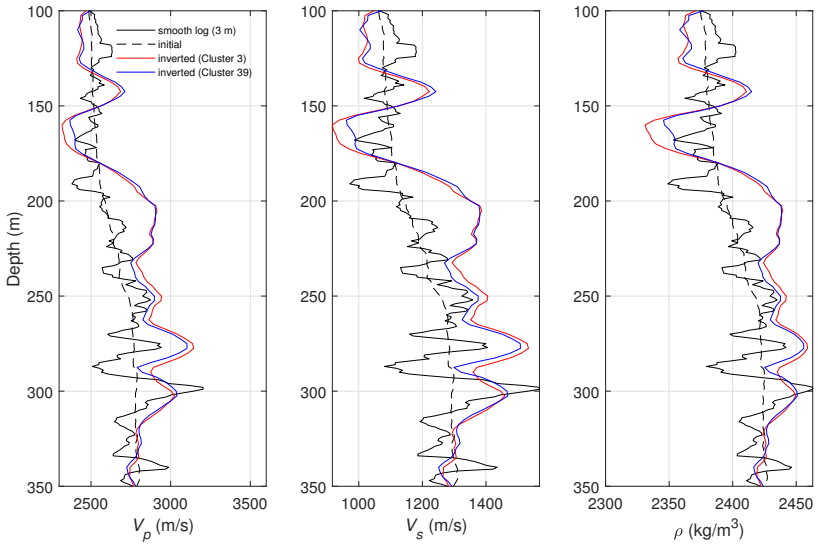

FIG. 18. The comparison of the initial and inverted velocities models with the well logs data.

The Figure 19 shows inverted models of V_{p}, V_{s}, and ρ for baseline data by multi-parameter FWI, where V_{p} and V_{s} are in good agreement with the inversion results in Figure 14, ρ is different from the inversion results in Figure 14. We use the multi-parameter inversion method, and Figure 20, Figure 21 and Figure 22 indicate inverted time-lapse V_{p}, V_{s}, ρ models for the other 9 selected monitor data in Figure 5, respectively. It can be seen from the Figure 21 and Figure 22, the time-lapse V_{p} and V_{s} anomaly located around 287.5 m, and the time-lapse ρ anomaly located at 300 m. Base on the phenomenon, we extract the time-lapse V_{p}, V_{s}, ρ model value for all 64 clusters (Figure 23). It can be seen that the inverted time-lapse V_{p} and V_{s} keep a good consistency with the phenomenon in Figure 17, while the inverted time-lapse ρ increases with the first $\mathrm{CO_2}$ injection, and then reaches a relatively stable stage, then decreases with the second $\mathrm{CO_2}$ injection, finally tries to return to initial state. The time-lapse V_{p}, V_{s} and ρ anomalies varies between 0 and -150 m/s, 0 and -120 m/s, and -2 to 20 $\mathrm{kg/m^3}$, respectively. The results of multi-parameter inversion have verified that V_{p} has a good correlation with V_{s}, while the correlation between ρ and V_{p} is not so high, which corresponds to the relationship diagrams in Figure 1 and Figure 2 .

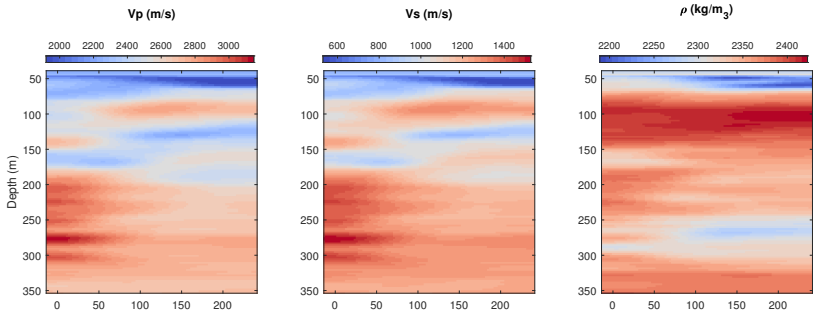

FIG. 19. The inverted V_{p}, V_{s}, and ρ models by multi-parameter inversion.

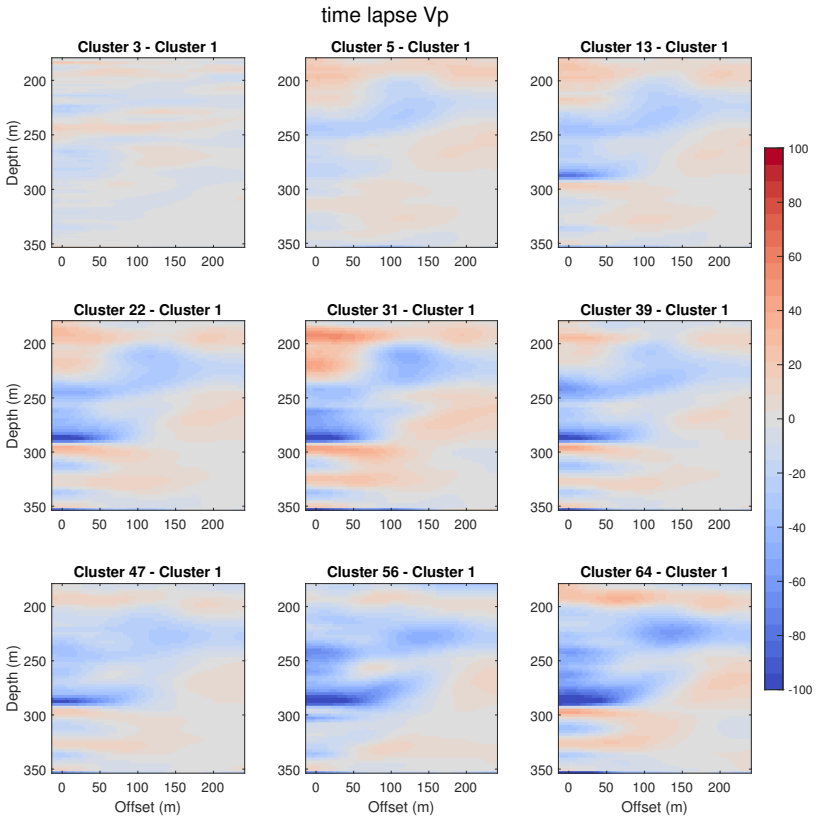

FIG. 20. The inverted V_{p} models difference between the 9 monitor data and baseline (multi-parameter inversion).

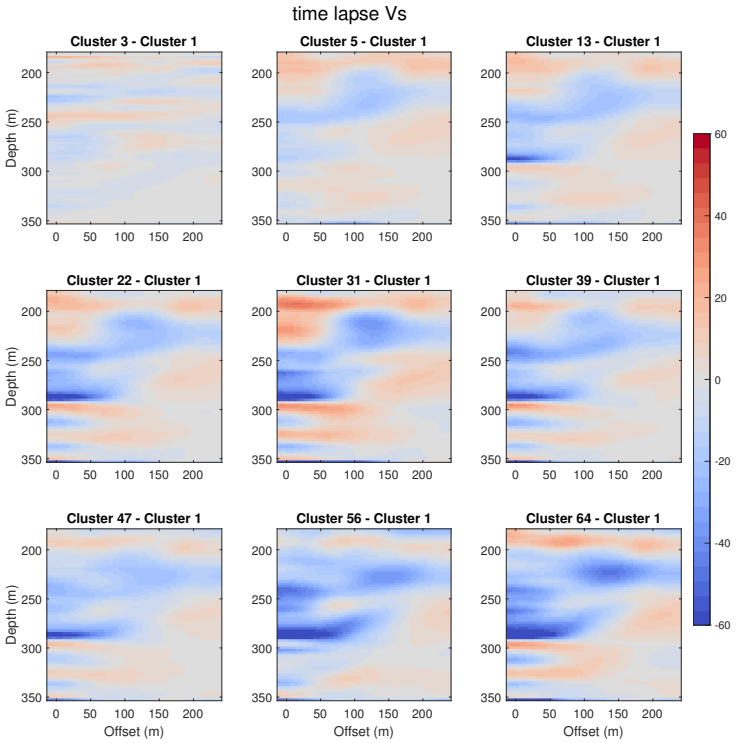

FIG. 21. The inverted V_{s} models difference between the 9 monitor data and baseline (multi-parameter inversion).

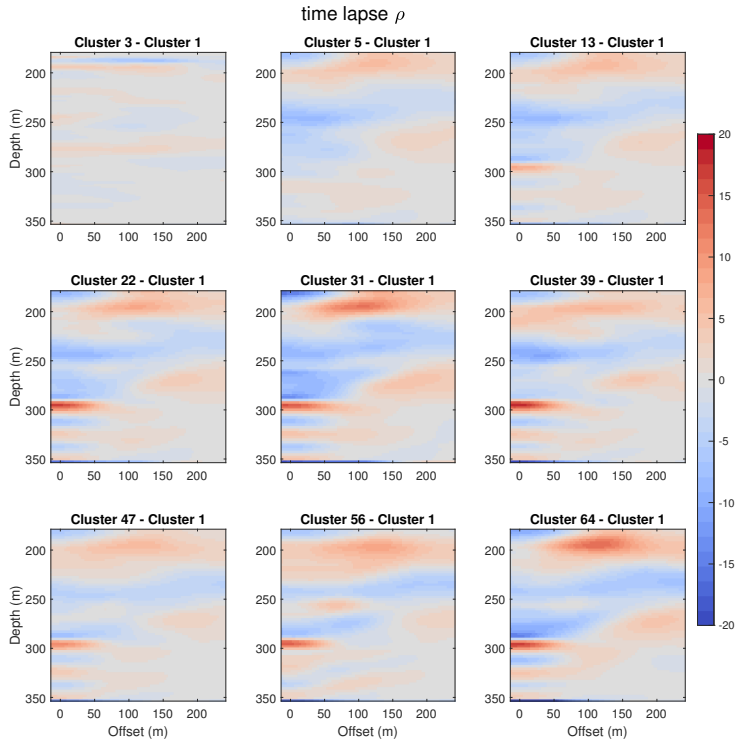

FIG. 22. The inverted ρ models difference between the 9 monitor data and baseline (multi-parameter inversion).

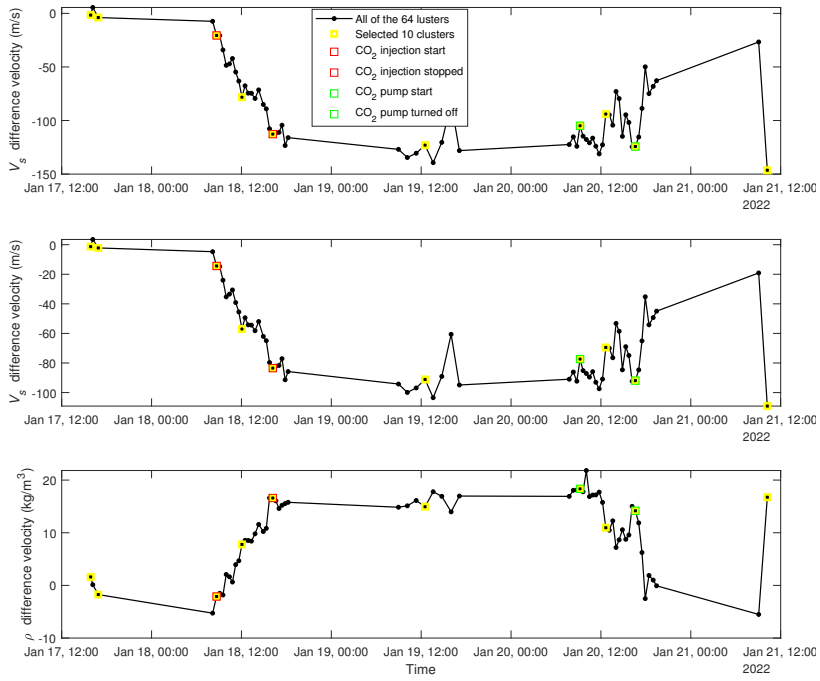

FIG. 23. The inverted models difference between the 64 clusters data and baseline by multi-parameter inversion. Top rows: The inverted V_{p} models difference at 287.5 m. Middle rows: The inverted V_{s} models difference at 287.5 m. Bottom rows: The inverted ρ models difference at 300 m. Yellow square are the 10 selected clusters. Red squares and green squares indicate the first and second CO_2 injection, respectively.

SYNTHETIC DATA TEST

In order to verify that the time-lapse anomalies identified by application of FWI to field data are indeed produced by reservoir changes, we conducted a test on a synthetic data. The test model size is 240 m in the x-direction and 350 m in the z-direction, and the space interval is 2.5 m. The well log located at (20 m, 80 m - 337 m). The baseline model has an anomaly at (40 m, 300 m) with a radius of 10 m. The background velocity is 3000 m/s and the anomaly velocity is 2775 m/s. The two monitor models have the same size and background velocity as the baseline model, and their the anomalies also located at (40 m, 300 m) with a velocity is 2625 m/s. The radii of anomalies of the monitor 1 model and the monitor 2 model are 10 m and 15 m, respectively. The shot offset is 215 m. The initial model is homogeneous model with velocity of 3000 m/s. Figure 24 shows the synthetic data inversion results. The true time-lapse anomaly velocity is -150 m/s, while time-lapse 1 anomaly is -120.22 m/s detected at (20 m, 300 m) and time-lapse 2 anomaly is -178.81 m/s detected at (40 m, 300 m). We can conclude that the time-lapse anomaly could also be detected by the single-source geometry, but the accuracy is affected by the anomaly size and velocity difference.

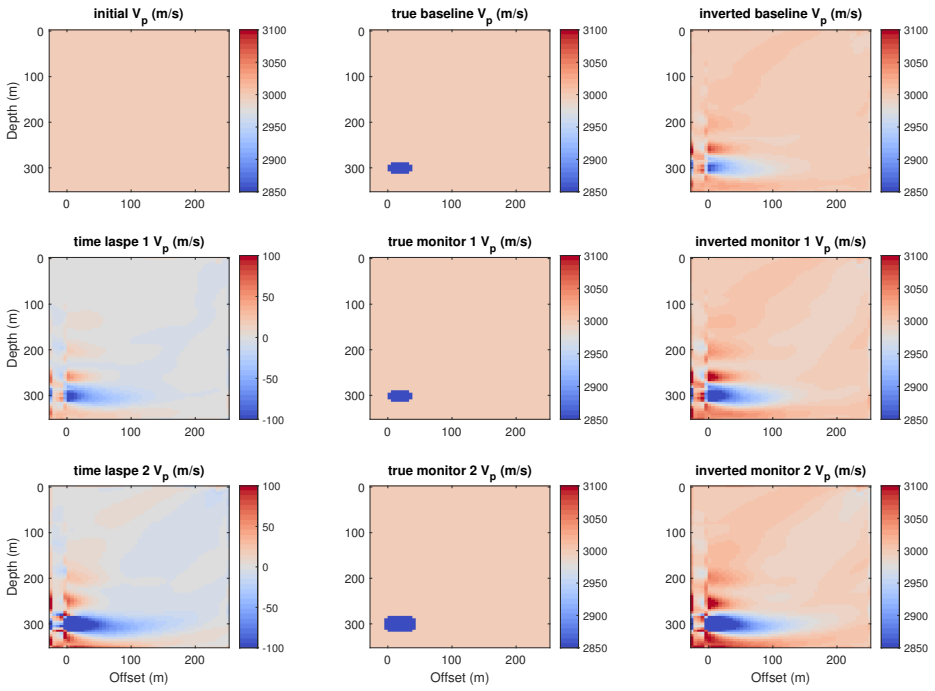

FIG. 24. Synthetic data inversion results.

CONCLUSIONS

We provide the rapid-repeat time-lapse velocity model inversion based on Tiny bubbles data. We use log-derived V_{p} parameterization to help model convergence and explain the data as a full multi-parameter inversion. We also performed the three-parameter time-lapse inversion to simultaneously quantify better anomaly in shear wave velocities and density. In addition, the effective source approach is introduced to avoid many complications in near-surface land seismic data. The results of 2D elastic FWI on field and synthetic offset VSP

data show that this technology can provide high-resolution models of physical properties of the subsurface, detecting and quantifying the anomaly. Our results show that FWI of VSP data is a suitable tool for the monitoring of CO_2 geosequestration and transportation.

ACKNOWLEDGMENTS

We thank the sponsors of CREWES for continued support. This work was funded by CREWES industrial sponsors and NSERC (Natural Science and Engineering Research Council of Canada) through the grant CRDPJ 543578-19. The data were acquired through a collaboration with the Containment and Monitoring Institute, Carbon Management Canada. Scott Keating was supported by the Canada First Research Excellence Fund, through the Global Research Initiative at the University of Calgary.

REFERENCES

Asnaashari, A., Brossier, R., Garambois, S., Audebert, F., Thore, P., and Virieux, J., 2015, Time-lapse seismic imaging using regularized full-waveform inversion with a prior model: which strategy?: Geophysical prospecting, **63**, No. 1, 78–98.

Cai, X., Innanen, K., Zhang, T., Eaid, M., Keating, S., Hall, K., and Lawton, D., 2022, Analysis of the fwi workflow for geophone and DAS data from the 2018 CaMI VSP survey: CREWES Research Reports.

Eaid, M., Keating, S., and Innanen, K., 2021a, Full waveform inversion of DAS field data from the 2018 CaMI VSP survey: CREWES Report.

Egorov, A., Pevzner, R., Bóna, A., Glubokovskikh, S., Puzyrev, V., Tertyshnikov, K., and Gurevich, B., 2017, Time-lapse full waveform inversion of vertical seismic profile data: Workflow and application to the co2crc otway project: Geophysical Research Letters, **44**, No. 14, 7211–7218.

Hu, Q., and Innanen, K., 2019, Rock physics analysis for the well-log data at CaMI FRS: CREWES Research Reports.

Innanen, K., Lawton, D., Hall, K., Bertram, K., and Bertram, M., 2019, Detection of transient time lapse seismic signatures associated with CO2 injection: CREWES Research Reports.

Isaac, J. H., and Lawton, D. C., 2016, Brooks revisited: CREWES Research Reports.

Keating, S., Eaid, M., and Innanen, K., 2021, Effective sources: removing the near surface from the vsp fwi problem: CREWES Report.

Pratt, R. G., 1999, Seismic waveform inversion in the frequency domain, part 1: Theory and verification in a physical scale model: Geophysics, **64**, No. 3, 888–901.

Roberts, M. A., Singh, S., and Hornby, B. E., 2008, Investigation into the use of 2d elastic waveform inversion from look-ahead walk-away vsp surveys: Geophysical prospecting, **56**, No. 6, 883–895.